Accounting for Changes in Radiation Improves the Ability of SIF to Track Water Stress-Induced Losses in Summer GPP in a Temperate Deciduous Forest

Zachary Butterfield[1], Troy Sehlin Magney[2], Katja Grossmann[3], Gil Bohrer[4], Christoph S. Vogel[1], Stephen Barr[1], and Gretchen Keppel-Aleks[1]

[1]University of Michigan-Ann Arbor
[2]California Institute of Technology
[3]University of Heidelberg
[4]Ohio State University

December 31, 2022

Abstract

As global observations of solar-induced chlorophyll fluorescence (SIF) have become available from multiple satellite platforms, SIF is increasingly used as a proxy for photosynthetic activity and ecosystem productivity. Because the relationship between SIF and gross primary productivity (GPP) depends on a variety of factors including ecosystem type and environmental conditions, it is necessary to study SIF observations across various spatiotemporal scales and ecosystems. To explore how SIF signals relate to productivity over a temperate deciduous forest, we deployed a PhotoSpec spectrometer system at the University of Michigan Biological Station AmeriFlux site (US-UMB) in the northern Lower Peninsula of Michigan during the 2018 and 2019 growing seasons. The PhotoSpec system consisted of two narrowband spectrometers, for the retrieval of SIF in the red (680-686 nm) and far-red (745-758 nm) regions of the electromagnetic spectrum, and a broadband spectrometer for the assessment of vegetation indices. We found that SIF correlated with GPP across diurnal and seasonal cycles, but that SIF irradiances were more strongly related to downwelling radiation than GPP. However, while this dependence of SIF on radiation obscured drought signals in SIF itself, we demonstrate that a SIF response to severe drought was apparent as a decrease in relative SIF. These results highlight the potential of SIF for detecting stress-induced losses in forest productivity. Additionally, we found that the red:far-red SIF ratio did not exhibit a response to drought stress, but was largely driven by seasonal and interannual changes in canopy structure, as well as by synoptic changes in downwelling radiation.

Hosted file

Accounting for Changes in Radiation Improves the Ability of SIF to Track Water Stress-Induced Losses in Summer GPP in a Temperate Deciduous Forest

Zachary Butterfield[1], Troy Magney[2], Katja Grossmann[3], Gil Bohrer[4], Chris Vogel[5], Stephen Barr[1], Gretchen Keppel-Aleks[1]

[1]Climate and Space Sciences and Engineering, University of Michigan, Ann Arbor, Michigan.

[2]Department of Plant Sciences, University of California, Davis, California.

[3]Institute of Environmental Physics, University of Heidelberg, Heidelberg, Germany.

[4]Civil, Environmental and Geodetic Engineering, Ohio State University, Columbus, Ohio.

[5]University of Michigan Biological Station, Pellston, Michigan.

Corresponding author: Zachary Butterfield (zbutterf@umich.edu)

Key Points:

- Solar-induced chlorophyll fluorescence above a temperate deciduous forest is more strongly tied to radiation than to productivity.
- Relative solar-induced fluorescence signals provide the strongest proxy for water stress-induced summer losses in productivity.
- The ratio of red to far-red solar-induced fluorescence is sensitive to phenological changes in canopy structure and downwelling radiation.

Abstract

As global observations of solar-induced chlorophyll fluorescence (SIF) have become available from multiple satellite platforms, SIF is increasingly used as a proxy for photosynthetic activity and ecosystem productivity. Because the relationship between SIF and gross primary productivity (GPP) depends on a variety of factors including ecosystem type and environmental conditions, it is necessary to study SIF observations across various spatiotemporal scales and ecosystems. To explore how SIF signals relate to productivity over a temperate deciduous forest, we deployed a PhotoSpec spectrometer system at the University of Michigan Biological Station AmeriFlux site (US-UMB) in the northern Lower Peninsula of Michigan during the 2018 and 2019 growing seasons. The PhotoSpec system consisted of two narrowband spectrometers, for the retrieval of SIF in the red (680-686 nm) and far-red (745-758 nm) regions of the electromagnetic spectrum, and a broadband spectrometer for the assessment of vegetation indices. We found that SIF correlated with GPP across diurnal and seasonal cycles, but that SIF irradiances were more strongly related to downwelling radiation than GPP. However, while this dependence of SIF on radiation obscured drought signals in SIF itself, we demonstrate that a SIF response to severe drought was apparent as a decrease in relative SIF. These results highlight the potential of SIF for detecting stress-induced losses in forest productivity. Additionally, we found that the red:far-red SIF ratio did not exhibit a response to drought stress, but was largely driven by seasonal and interannual changes in canopy structure, as well as by synoptic changes in downwelling radiation.

Plain Language Summary

Satellite measurements of solar-induced chlorophyll fluorescence (SIF), a faint light signal emitted from vegetation during photosynthesis, are increasingly being used to estimate ecosystem productivity and carbon uptake. To accurately do so requires a robust understanding of how the relationship between SIF and plant productivity changes over time, in response to environmental stressors, and across different ecosystems. To better understand SIF signals and how they relate to carbon uptake over a temperate deciduous forest, we used a high-precision spectrometer system to observe SIF signals at an AmeriFlux site (US-UMB) in the northern Lower Peninsula of Michigan. While the shared dependence of SIF and ecosystem productivity on sunlight lead to strong daily and seasonal correlations, we found that SIF signals were more closely tied to the amount of incoming sunlight than to ecosystem productivity. Despite the stronger dependence of SIF on sunlight, we show that drought conditions lead to a lower SIF relative to the total light signal. Lastly, we show that the observation of SIF at multiple wavelengths may provide additional information on seasonal and interannual changes in canopy structure. Our results demonstrate the value and limitations in using SIF to assess carbon dynamics over temperate deciduous forest ecosystems.

1 Introduction

Global ecosystems currently provide a sink for roughly one quarter of anthropogenic carbon emissions (Friedlingstein et al., 2022), and the climate-driven variations in this carbon sink therefore have significant implications for long-term changes in climate. Direct quantification of net and gross ecosystem productivity at regional to global scales is elusive, however, given the spatial heterogeneity of the global land surface and the sparse nature of direct observations of land-atmosphere carbon exchange, and contributes significant uncertainty to the global carbon budget (Friedlingstein et al., 2022; le Quéré et al., 2018).

The unique challenges involved in quantifying the biospheric carbon sink at the global scale underscore the need for satellite-based observations that allow for the inference of ecosystem productivity across a variety of ecosystems and spatiotemporal scales. Traditionally, optical indices such as the normalized difference vegetation index (NDVI) have been used to quantify ecosystem productivity (Tucker, 1979). These signals represent the 'greenness' of vegetation which relates to the amount of light absorbed by vegetation, and empirically correlate with productivity across spatial gradients. However, vegetation indices lack a direct mechanistic relation with the short-term variations of photosynthetic rates, and thus require ancillary meteorological data to account for environmental stressors and to estimate light use efficiency (LUE), which is the efficiency at which sunlight is used to drive photochemistry and carbon fixation (Running et al., 2004). Additionally, vegetation indices can be vulnerable to saturation effects (X. Yang et al., 2015) or influenced by factors unrelated to vegetation, such as snow cover (Beck et al., 2006).

Solar-induced chlorophyll fluorescence (SIF) is a newer space-based proxy for terrestrial photosynthesis (Frankenberg, Butz, et al., 2011). As leaves absorb solar photons for use in photosynthesis, photons not used for photochemistry are either dissipated as heat via non-photochemical quenching (NPQ) or are fluoresced back to the environment as SIF. SIF, therefore, is directly related to activity of the photosynthetic machinery, as it represents an emission of red and far-red photons from the photosystems. Satellite observations of far-red SIF have been shown to scale with spatial and seasonal patterns of gross primary productivity (GPP; Frankenberg, Fisher, et al., 2011; Sun et al., 2017), indicating a potential for SIF as a direct proxy of carbon uptake through photosynthesis. There has been a recent proliferation of satellite-based observations of far-red SIF (Frankenberg et al., 2014; Joiner et al., 2013; Köhler et al., 2018) and, more recently, red SIF (Köhler et al., 2020; Wolanin et al., 2015). Quantitative assessments of SIF signals across a range of ecosystems and spatial and temporal scales are needed to inform the interpretation of these data.

The strong relationship between SIF and GPP stems in part from a shared dependence on solar radiation (Magney et al., 2020). Top-of-canopy SIF can be expressed as:

$$\mathrm{SIF} = \mathrm{PAR} \times \mathrm{fPAR} \times \mathrm{SIF}_{yield} \times f_{esc} \tag{1}$$

(Zeng et al., 2019) where fluorescence yield (SIF_{yield}) represents the efficiency at which the photosystems emit photons, photosynthetically active radiation (PAR) indicates downwelling radiation available for photosynthesis, and fPAR indicates the fraction of PAR absorbed by the canopy, which depends primarily on green leaf area, chlorophyll content, and canopy structure. The fluorescence escape ratio (f_{esc}) represents the fraction of total emitted fluorescence that escapes the top of canopy and can be detected remotely, rather than being deflected or reabsorbed by leaves deeper within the canopy (Dechant et al., 2020; Zeng et al., 2019). Similarly, GPP can be expressed as the product of PAR, fPAR, and LUE (X. Yang et al., 2015):

$$\mathrm{GPP} = \mathrm{PAR} \times \mathrm{fPAR} \times \mathrm{LUE} \tag{2}$$

As LUE is the most difficult component of GPP to estimate using remote sensing and is traditionally inferred from models (Gitelson & Gamon, 2015; Monteith, 1977), there is much interest in characterizing its relationship with SIF (and SIF_{yield}, or the rate at which absorbed photons are fluoresced as SIF). X. Yang et al. (2015) showed that SIF contained some information about LUE over a temperate deciduous forest, by dividing tower-based SIF by total absorbed PAR to reveal a weak correlation between LUE and SIF_{yield}, although this relationship was weaker than the correlation between far-red SIF and GPP.

Magney, Bowling, et al. (2019) and Pierrat et al. (2022) further showed a strong relationship between SIF and GPP in northern evergreen forests under minimal changes in canopy structure and absorbed PAR, when more traditional observations such as NDVI, which are closely tied to changes in chlorophyll content, did not capture seasonal productivity dynamics. The demonstrated seasonality in SIF, even when greenness remains constant, suggests that the SIF signal is sensitive to seasonal changes in photoprotective pigments and LUE, and therefore provides a more robust proxy of GPP than greenness alone.

Despite the strong correlations reported between SIF and GPP at seasonal and diurnal timescales, uncertainties remain in the mechanistic relationship between SIF and GPP (Ryu et al., 2019), and in how that relationship changes across different ecosystems and spatiotemporal scales. Several studies have found that SIF over cropland is more closely tied to absorbed PAR (APAR) than to GPP (Miao et al., 2018; K. Yang et al., 2018; Yazbeck et al., 2021), and Zeng et al. (2019) broadly demonstrated that SIF is strongly influenced by canopy structure and changes in f_{esc}. SIF is also dependent on the fluorescence yield of the photosystems. Furthermore, while GPP is sensitive to ecosystem stress through changes in LUE, it is not understood how fluorescence yield, and therefore observed SIF, responds to stress-induced changes. It is therefore unclear how closely the SIF response to environmental stressors mirrors changes in GPP. Several satellite-based studies have used SIF to observe the impacts of moderate to severe drought (Li et al., 2020; Song et al., 2018; Yoshida et al., 2015); nonetheless, observations of SIF tend to be less sensitive to interannual variability in GPP during summer and may not show the impacts of mild stress (Butterfield et al., 2020). Furthermore, Yazbeck et al. (2021) demonstrated that SIF did not reliably capture daily-scale reductions in GPP due to water stress at multiple flux tower sites. Wohlfahrt et al. (2018) showed that local scale observations of SIF over a Mediterranean pine forest decoupled from GPP under environmental stress and suggested that much of the strong correlation between SIF and GPP in this ecosystem was driven by a shared dependence on APAR, calling into question the detectability of stress-induced changes in GPP from SIF observations. However, they also noted an increase in the red:far-red SIF ratio aligning with peak stress conditions. The differing behaviors of red and far-red SIF signals during an ecosystem stress event warrant further investigations into what can be learned from simultaneous observations of SIF at both red and far-red wavelengths.

To assess the relationship between SIF and GPP and their responses to environmental variables and stressors, we deployed a tower-based PhotoSpec spectrometer system (Grossmann et al., 2018) above a temperate deciduous forest within the footprint of the US-UMB flux tower at the University of Michigan Biological Station. We present results from two years of growing-season observations, during which we collected red and far-red SIF observations at a high temporal frequency (~20 s), providing an opportunity to quantify diurnal and intraseasonal variation in the SIF signal. Our goals were to: 1) explore the dependence of SIF on downwelling PAR and test how this dependence influenced the ability of SIF to track intraseasonal changes in GPP; 2) characterize the relationship between SIF and GPP and test how it changed over the course of the growing season and during periods of water stress; and 3) explore the behavior of the red:far-red SIF ratio and assess its response to changes in environmental conditions.

2 Data and Methods

2.1 Study Location at University of Michigan Biological Station

We obtained data at the University of Michigan Biological Station site within a deciduous broadleaf forest composed primarily of aspen, oak, maple, beech, and some understory pine, with a canopy height of approximately 22 m. The forest age is roughly one century as widespread fires burned much of the region in the early twentieth century. The site is characterized by sandy soil, with rapid percolation of rainfall to deep soil layers. This location was chosen in part because it is a well-studied forest ecosystem, with long-standing eddy covariance-based observations of water and carbon fluxes (Frasson et al., 2015; Gough et al., 2013, 2022), canopy structure (Fotis et al., 2018), soil moisture (He et al., 2014), and sap flow and tree hydrology (Aron et al., 2019; Matheny et al., 2014, 2017).

2.2 PhotoSpec Tower-Based Observations

We built and deployed a PhotoSpec spectrometer system (Grossmann et al., 2018) at the US-UMB tower during the 2018 and 2019 growing seasons (Butterfield et al., 2022). The PhotoSpec system consisted of two narrowband spectrometers (QEPro, Ocean Optics Inc.): one with a wavelength range of 670-732 nm and a resolution of 0.074 nm/pixel, 0.3 nm full width half maximum (FWHM), for measuring SIF in the red region of the spectrum, and a second QEPro (729-784 nm, 0.067 nm/pixel, 0.3 nm FWHM) optimized for measuring SIF in the far-red. An additional broadband spectrometer (Flame, Ocean Optics Inc.; 177-874 nm, 0.382 nm/pixel, 1.2 nm FWHM) permitted the calculation of vegetation indices, such as NDVI, from the measured spectra. A 2-D scanning telescope was mounted on the US-UMB tower at a height of 45 m and could point at various locations in the canopy using a narrow field of view (about 0.7°). Light from the canopy was thus directed through a fiber optic cable, and subsequently split as input to the three spectrometers.

We acquired automated observations in three azimuthal directions: 60° east of south, due south, and 60° west of south. For each azimuth angle, we acquired data along an elevation transect by scanning from 90° (nadir) to 45° below the horizon. For each individual location along the transects, we optimized the exposure times for the spectrometers to maintain consistent detector signal level. Multiple exposures were then integrated together into 20 s measurements before moving the telescope to the next location. Observations were collected when the solar elevation angle was > 10° and solar reference spectra were collected at least every 10 measurements using an upward-facing diffuser disk. To ensure that observations included green vegetation and were of sufficiently high quality, data were further filtered to only include retrievals where NDVI was > 0.2, red and far-red SIF retrieval errors were < 0.1 mW m^{-2} sr^{-1} nm^{-1}, and SIF irradiances were calculated to be between -0.1 and 10 mW m^{-2} sr^{-1} nm^{-1} and between -2 and 20% of the total light signal. These filters resulted in the removal of ~12% of collected data. A full cycle through the three azimuth angles took approximately 90 minutes; therefore, after removing outlier data, we used 90-minute averages for sub-daily comparisons.

The uncertainty of each 90-minute period was calculated as the standard deviation of included observations.

SIF irradiances were calculated from the QEPro spectra for both the red (680-686 nm) and far-red (745-758 nm) regions of the electromagnetic spectrum using a physical retrieval based on the infilling of solar Fraunhofer lines (Grossmann et al., 2018). To isolate SIF signals from their dependence on PAR, we calculated relative SIF by dividing the observed SIF irradiance by the total reflected and fluoresced irradiance at the respective wavelength to represent SIF as a percentage of the total light signal. We calculated NDVI, the photochemical reflectance index (PRI), which is sensitive to de-epoxidation of xanthophyll cycle pigments and light use efficiency (Gamon et al., 2001), and a chlorophyll index (Chlorophyll_{RS}; Magney, Frankenberg, et al., 2019; Datt, 1999) using spectra from the broadband Flame spectrometer (Text S1). While our site did not include direct observations of fPAR, we assume a rough proportionality between NDVI and fPAR (Running et al., 2004) from which we inferred the qualitative seasonal behavior of fPAR (i.e., we assumed that seasonal changes in fPAR tracked seasonal changes in NDVI).

The SIF observations were radiometrically calibrated using a second broadband Flame spectrometer with a cosine corrector (CC-3-UV-S, Ocean Optics Inc.) that was calibrated using radiometric standard lamp (HL-3-P-CAL, Ocean Optics Inc.). We recorded simultaneous measurements alongside the PhotoSpec instrument with the second Flame spectrometer using a reflective calibration disk (Spectralon Diffuse Reflectance Standard, Labsphere Inc.) at least once per growing season whenever any adjustments were made to the optical components. Between the 2018 and 2019 growing seasons, radiometric calibration coefficients remained within 2.5 and 1% for red and far-red SIF retrievals, respectively. Wavelength calibrations were done using a Mercury-Argon lamp (HG-1, Ocean Optics Inc.).

2.3 AmeriFlux and Meteorological Data

For this study, we compared PhotoSpec SIF data with ecosystem flux observations from the AmeriFlux tower (46 m above ground), from which CO_2 and H_2O flux data have been observed since 1999 (Gough et al., 2022). Eddy covariance (EC) flux observations of Net Ecosytem Exchange (NEE) were partitioned into estimates of ecosystem respiration (RE) and GPP, from which we used the processed half-hourly estimates of GPP from April 2018 through November 2019. We used the data from 2007-2019 for a baseline comparison with a multi-year mean. In addition to GPP flux data, we used coincident meteorological observations from the same AmeriFlux dataset. These included air temperature, precipitation, vapor pressure deficit (VPD), volumetric soil water content (SWC) at a depth of 30 cm, and downwelling PAR. Data for the site was obtained through the AmeriFlux database (AmeriFlux site ID: US-UMB; Gough et al., 2022). More details about the data processing approach for this site are described by Gough et al. (2013).

Flux data were processed by the site team following the standard EC processing protocol (Rebmann et al., 2012). Flux data during periods of low turbulent mixing were filtered using the u*-filter threshold approach, with the threshold values calculated seasonally following Reichstein et al. (2005). Filtered nighttime NEE observations were assumed to represent RE, and seasonal nighttime RE observations were then used to train an automated neural network model

(ANN; see Morin et al., 2014) to infer daytime RE using time of day, air temperature, vapor pressure deficit, soil temperature, and soil moisture as inputs (Lasslop et al., 2010). For all ANN models, 50% of the data were used for training, 25% for evaluation and 25% for validation of the ensemble's goodness of fit. The ensemble mean of the best-performing 10% of 1000 ANN models was used to predict RE during the day, and during nighttime observation gaps. GPP was assumed to be zero during winters and overnight, and daytime GPP during the growing season was calculated as the difference between observed NEE and modelled RE. ANN models with a setup similar to the one used for RE were used to model GPP and gapfill missing daytime observations during the growing season. The GPP ANN models used air temperature, incoming PAR, relative humidity, vapor pressure deficit, sensible and latent heat fluxes, and soil moisture as input variables.

We aggregated the half-hourly AmeriFlux data to 90-minute and daily values for each variable either by simple summation (precipitation) or averaging (other variables). As NDVI (and therefore fPAR) was generally constant between leaf out and senescence, we calculated an LUE proxy as GPP/PAR (Gitelson & Gamon, 2015). Seasonal estimates for species-specific maximal leaf area index (LAI) at the site were measured using samples collected with leaf litter traps.

2.4 Satellite Observations of SIF from OCO-2

We compared satellite-based observations of SIF from the Orbiting Carbon Observatory-2 (OCO-2; Science Team et al., 2017; Yu et al., 2019) with our tower-based PhotoSpec observations. OCO-2 is a polar orbiting satellite with a local overpass time of 1:30pm. SIF was retrieved from OCO-2 spectra at 757 nm and 771 nm using a non-linear least-squares approach to evaluate the infilling of solar Fraunhofer lines (Sun et al., 2018). We averaged OCO-2 SIF retrievals at 757 nm (which was within our far-red fitting window of 745-758 nm) that fell within a one-degree grid cell centered at US-UMB. Individual soundings were converted to daily-averages using a clear-sky PAR proxy, which uses the cosine of the solar zenith angle to account for diurnal variability in the SIF signal. We subsequently calculated a single mean and standard deviation of OCO-2 observations for each day with available overpass data, resulting in nine individual data points throughout the 2018 and 2019 growing seasons. We then tested the linear correlation of these data with corresponding daily means observed using the PhotoSpec instrument.

3 Results

3.1 Climatological Context for 2018-2019 Growing Seasons

The 2018 and 2019 growing seasons were both more productive than the 2007-2019 mean based on eddy covariance GPP data (Figure 1a). In 2018, growing season onset was delayed by about a week relative to the multi-year mean, but GPP increased rapidly (~0.5 μmol m^{-2} s^{-1} day^{-1}) throughout the second half of May during a period with above average temperatures (Figure 1a-b). GPP reached a seasonal peak value of about 10 μmol m^{-2} s^{-1} in late June, roughly 25% higher than the multi-year mean, and remained higher than average until mid-August. In 2019, onset of the growing season occurred even later, following the multi-year mean by about 2 weeks, due to very wet and cold spring conditions (Figure 1b-c). GPP subsequently reached a peak value of > 12 μmol m^{-2} s^{-1} day^{-1} in late July, 50% higher than the multi-year mean, and remained nearly a standard deviation higher than average until September (Figure 1a).

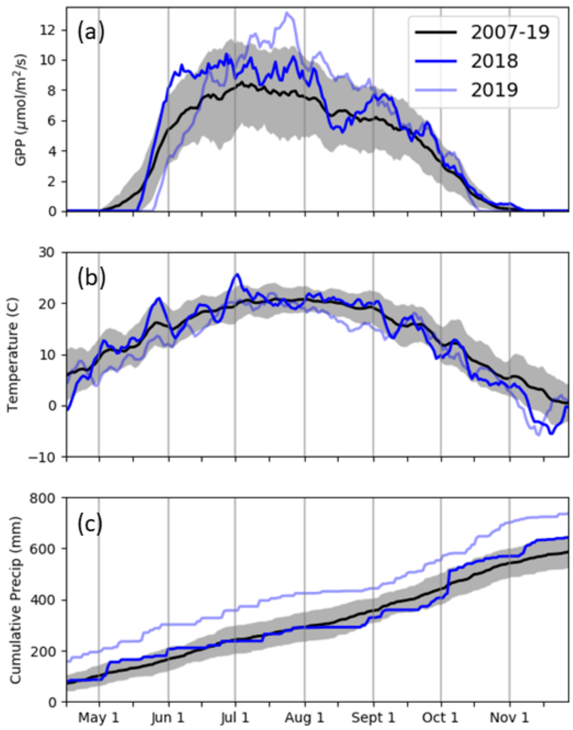

Figure 1. Observations of GPP (a), temperature (b), and cumulative precipitation (c) at US-UMB during the 2018 (dark blue) and 2019 (light blue) growing seasons. The 2007-2019 multi-year mean for each panel is included as a black line, with shading representing ±1 standard deviation. GPP and temperature are plotted as 7-day running means.

Both 2018 and 2019 experienced water stress-induced declines in GPP during late summer that occurred with moderate to severe drought conditions as classified by the U. S. Drought Monitor (USDM; Svoboda et al., 2002; accessed via http://droughtmonitor.unl.edu). The USDM classification showed a severe drought in mid-August 2018 that followed a series of three dry spells in early June, early July, and August (Figure 1c). While the first of these dry periods did not lead to dry soil moisture conditions, the cumulative influence of the two later dry periods led to soil water content falling to ~5% and coincided with local maxima in VPD upwards of 9 hPa (Figure 2g). GPP levels were relatively robust during the first period of dry soil conditions from late June through July 11, but during the second dry period from late July through August 18, productivity ultimately declined by about 30%, to levels below the multi-year mean. Towards the end of August, GPP recovered back to about 20% above the climatological mean. GPP may be increasingly sensitive to dry soil conditions over the growing season due to the fact that the soil matric potential can continue to increase even as SWC asymptotes to a lower limit (Köcher et al., 2009; Lascano et al., 2007). The soil matric potential reflects soil hydraulic tension, which at higher values indicates greater resistance to vegetation taking up water through their roots. Late summer declines in GPP occur roughly every other year at the US-UMB site and are not always tied to an obvious drought signal (Figure S1). While 2019 was not characterized by any periods of severe drought stress, GPP observations did decrease in late July from about 50% to only 20% above the climatological mean (Figure 1a). This decline in productivity coincided with decreasing SWC (Figure 2h) and little accumulated precipitation (Figure 1c), but also with cooler temperatures (Figure 1b) and only a slight increase in VPD (Figure 2h).

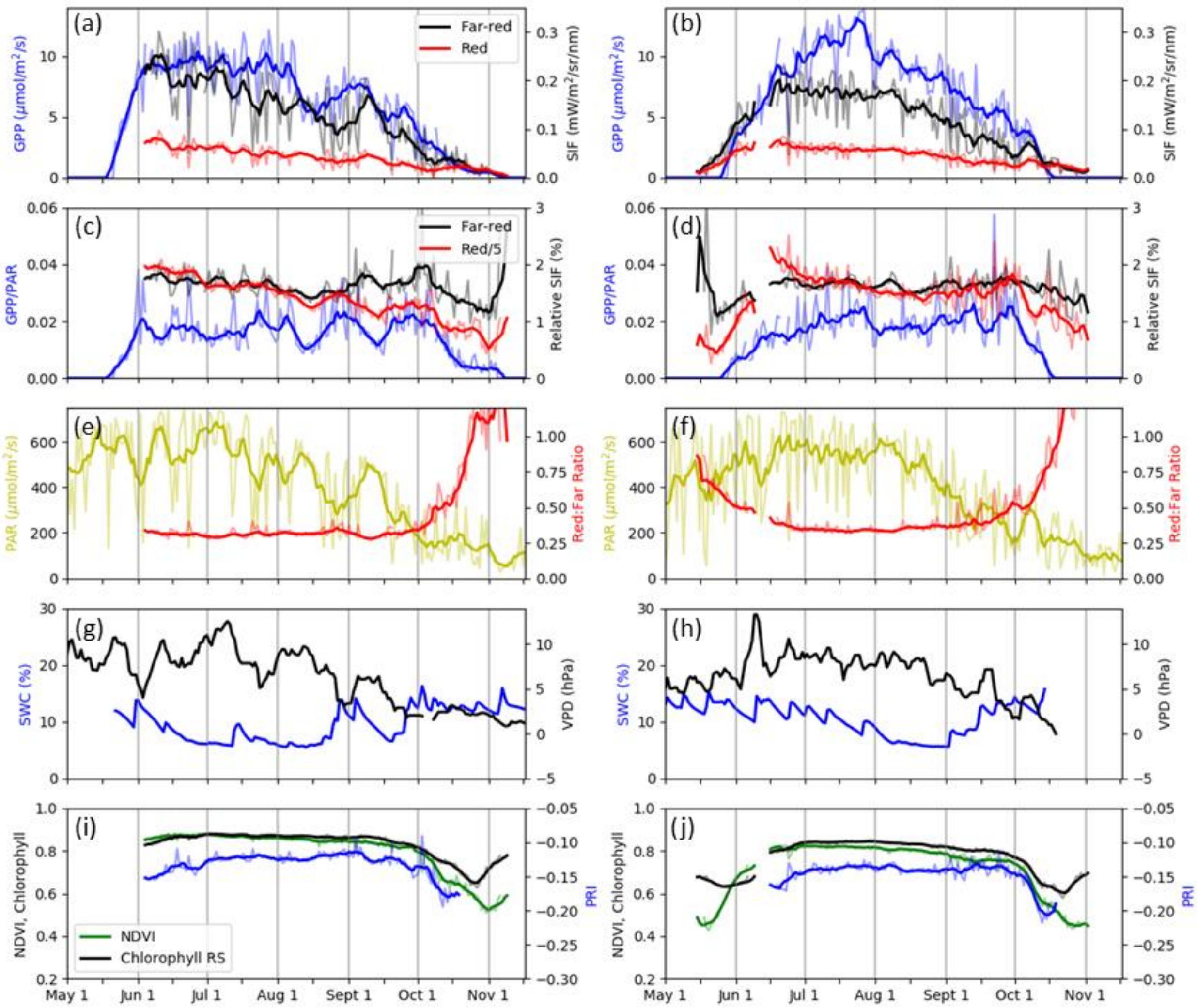

Figure 2. Growing season time series of GPP and SIF irradiance (a, b), GPP/PAR and relative SIF (c, d), photosynthetically active radiation (PAR) and the red:far-red SIF ratio (e, f), soil water content (SWC) and vapor pressure deficit (VPD (g, h), and NDVI, Chlorophyll$_{RS}$, and PRI (i, j) during 2018 (left) and 2019 (right). With the exception of SWC and VPD, bold lines represent the 7-day running mean of daily-averaged data (thin lines).

3.2 Characteristics of Red and Far-red SIF Signals

Far-red SIF observations during 2018 and 2019 generally followed a seasonal cycle similar to that of GPP (Figure 2a-b). Both SIF and GPP reached peak levels in early summer and steadily declined throughout late summer and fall. The red SIF signal followed a similar pattern but exhibited relatively higher values in early spring and fall (Figure 2a-b), illustrated by higher red:far-red SIF ratios during the shoulder seasons (Figure 2e-f) corresponding with low NDVI and Chlorophyll$_{RS}$ values (Figure 2i-j). This contrast between red and far-red SIF seasonality results from top-of-canopy red SIF observations being more sensitive to canopy structure and chlorophyll content (Magney, Frankenberg, et al., 2019), since a smaller fraction of total emitted SIF is scattered or reabsorbed by the canopy during the springtime when the canopy is not yet fully developed or as chlorophyll content decreases in fall. This dependence is also evident in lower red:far-red SIF ratios in 2018, concurring with differences in other observations including NDVI (maximum value of 0.88 in 2018 and 0.84 in 2019) and LAI, where measurements using leaf litter traps showed almost a 20% reduction in 2019 compared to 2018 (4.38 in 2018 versus 3.64 in 2019; Table 1). The lower red:far-red SIF ratio in 2018, when LAI was high, corroborates the hypothesis that a denser canopy limits top-of-canopy red fluorescence. Taken together, these differences in the behavior of SIF at different wavelengths suggested that far-red SIF better reflected the seasonal cycle of productivity in a temperate deciduous forest, and that red SIF was more sensitive than far-red SIF to seasonal, and potentially interannual, changes in canopy structure and chlorophyll concentration.

Table 1. Species-specific leaf area index (LAI) values as observed at the US-UMB AmeriFlux site for 2018 and 2019 using leaf litter traps.

Species	**2018 LAI**	**2019 LAI**
Bigtooth aspen (*Populus grandidentata*)	1.286	0.981
Red maple (*Acer rubrum*)	0.891	0.730
American beech (*Fagus grandifolia*)	0.292	0.281
Red oak (*Quercus rubra*)	1.073	0.878
Paper birch (*Betula papyrifera*)	0.238	0.178
White pine (*Pinus strobus*)	0.587	0.578
Red pine (Pinus resinosa)	0.008	0.011
Total	**4.375**	**3.636**

We calculated correlations between SIF and GPP with data aggregated to 90-minute, daily, and weekly timescales (Figure 3). For far-red SIF, weekly-aggregated data had the highest correlation with GPP (R^2 = 0.81), while 90-minute- and daily-aggregated data had R^2 values of 0.61 and 0.62, respectively. The correlations between GPP and red SIF were weaker (R^2 values of 0.56, 0.54, and 0.72 for 90-minute, daily, and weekly timescales; Figure S2). Over the growing season, weekly values of far-red SIF span the range from near zero during the early and late growing season, to 0.2 mW m^{-2} sr^{-1} nm^{-1} during peak growing season in July (Figure 3d). Daily values during the month of July, in contrast, have a standard deviation of ~0.05 mW m^{-2} sr^{-1} nm^{-1} and reach as high as 0.3 mW m^{-2} sr^{-1} nm^{-1} (Figure 3c), suggesting that cloud-driven variability in PAR may be a significant driver in far-red SIF variability while GPP in this ecosystem may be less sensitive to day-to-day variability in light availability.

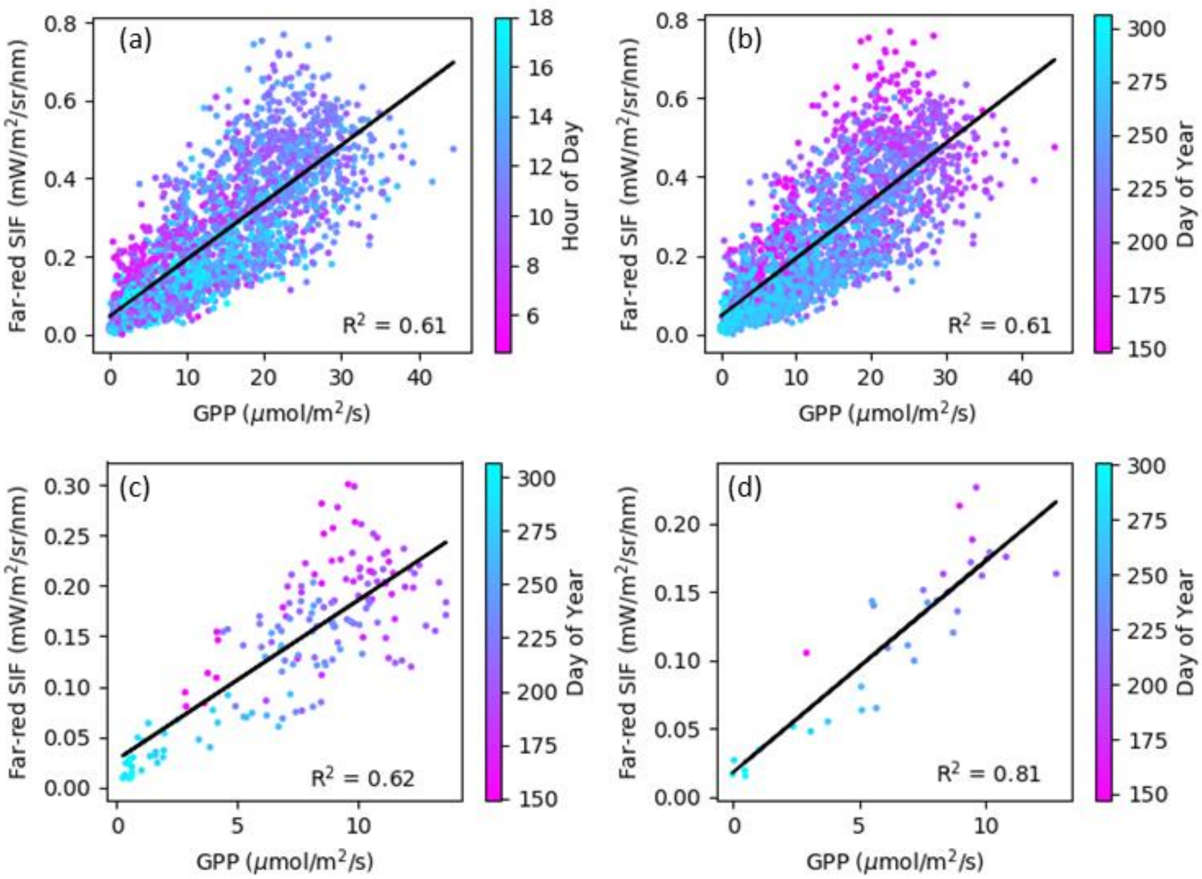

Figure 3. Correlation between far-red SIF and GPP, temporally aggregated to 90-minute (a, b), daily (c), and weekly (d) resolutions. Color bars indicate hour of day (a) or day of year (b-d).

To investigate how seasonal changes influence the relationship between GPP and far-red SIF we fit linear correlations to data within individual months for 2018 and 2019 (Figure 4). We quantified uncertainties both on slopes and R^2 values using a bootstrapping approach in which we sampled the monthly data with replacement. Results for daily-averaged data confirmed that GPP and far-red SIF are best correlated during spring and fall, when seasonal phenological changes in the deciduous forest result in a large dynamic range in fPAR (using NDVI as a proxy). Shared dependence on fPAR between SIF and GPP thus lead to stronger correlations during these months (Figure 4d; discussed in more detail in section 4.1). Correlations between 90-minute data showed that the inclusion of diurnal variations led to consistently stronger correlations throughout the summer (Figure 4b). The resulting slopes from the linear fits of daily data exhibited large uncertainties and do not exhibit obvious changes over the course of the growing season (Figure 4c). Linear fits of 90-minute data were better constrained to the origin by including near-zero values in morning and evening, resulting in more precise slopes (Figure 4a). These results showed that the far-red SIF:GPP slope was highest during the spring and declined over the course of the growing season (Figure 4a; further discussed in Section 4.2).

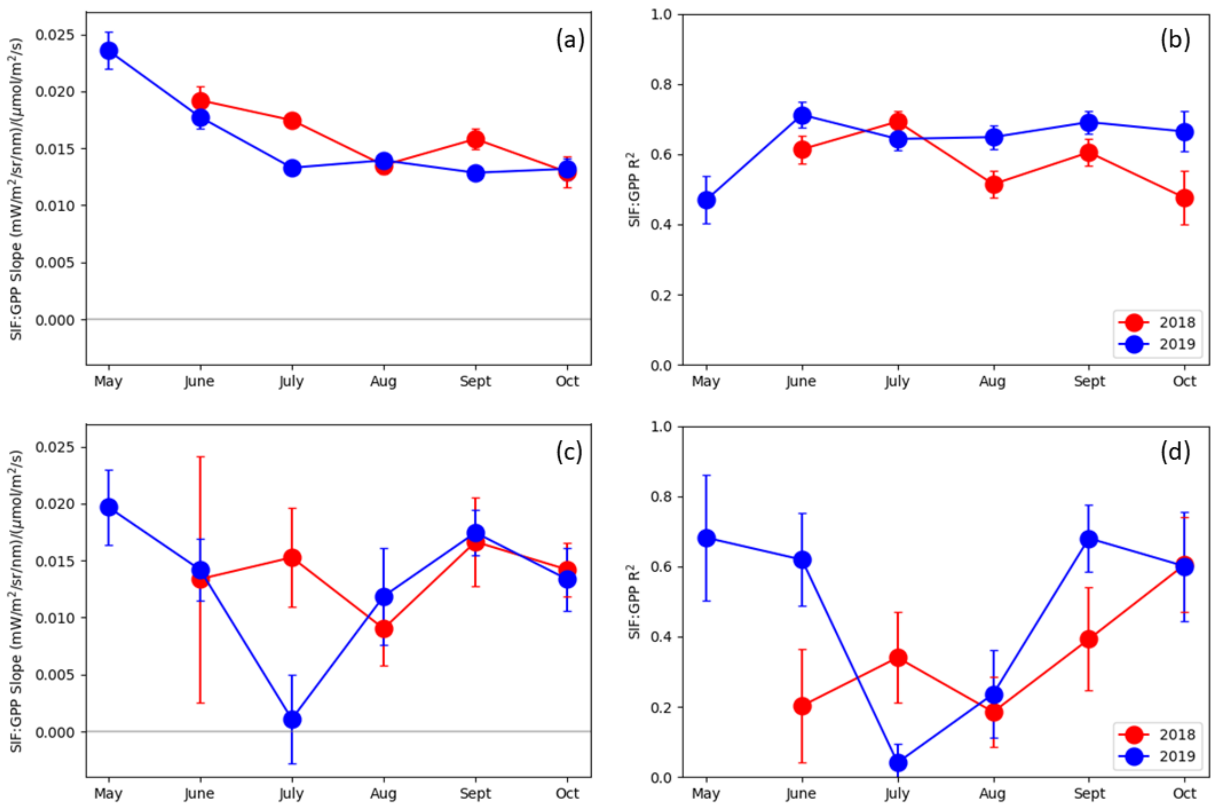

Figure 4. Slopes and R^2 values from monthly linear regressions of 90-minute- (a, b) and daily-averaged (c, d) far-red SIF with GPP. Data from 2018 are in red, while 2019 data are in blue. Error bars represent the standard deviations of results from a bootstrapping method used to test the robustness of the linear regressions.

While both SIF and GPP depend on PAR (Equation 1 and 2), SIF was more tightly coupled to downwelling PAR than was GPP at our site (Figure 5). Without direct observations of fPAR, we assumed that fPAR was near constant under peak growing season conditions when NDVI was stable (see Running et al., 2004; Figure 2i-j), and that the relationship during summer between SIF and PAR were therefore indicative of the relationship between SIF and APAR. The close dependence of SIF on radiation was illustrated by shared temporal patterns of SIF and PAR throughout summer (Figure 2a-b, e-f), and by a strong correlation between daily-aggregated far-red and red SIF with PAR (R^2 = 0.90, Figure 5a, S3). GPP and PAR exhibited a much weaker correlation (R^2 = 0.51; Figure 5b). Monthly correlations of far-red SIF and GPP with PAR confirmed that GPP exhibits a weaker relationship with downwelling PAR than SIF (Figure S4b, d). Monthly correlations also showed that the relationship between SIF and PAR was weakest during spring and fall (Figure S4d) when variations in NDVI (and fPAR), due to rapid changes in the canopy (i.e. leaf-out and senescence), cause APAR to deviate qualitatively from PAR. Lower NDVI (and fPAR) during spring and fall also led to lower values of SIF and GPP relative to PAR (Figure S4a, c), as a smaller fraction of downwelling radiation is absorbed by vegetation during these periods.

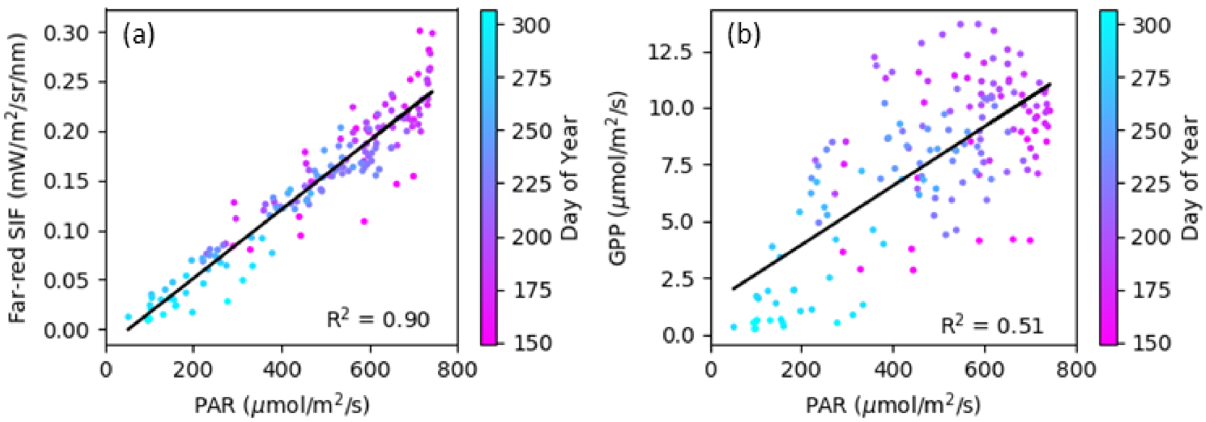

Figure 5. Correlation between daily-averaged far-red SIF (a) and GPP (b) with photosynthetically active radiation (PAR). Color bars are weighted by day of year.

We calculated relative SIF, or SIF as a fraction of the total light signal, in order to decouple the SIF signal from its dependence on PAR (Figure 2c-d). During peak summer conditions, relative far-red SIF typically was just under 2% of total observed light, while relative red SIF was 5-10%. Red and far-red relative SIF exhibited lower values during early spring and late fall, when the ecosystem absorbs less downwelling radiation for photosynthesis. We calculated an LUE proxy as GPP divided by PAR and found that relative far-red and especially red SIF visually track intraseasonal patterns in LUE (Figure 2c-d), notably during the August 2018 severe drought. Relative red SIF shares a similar seasonal pattern with GPP/PAR, leading to a stronger correlation between daily-aggregated data (R^2 = 0.34; Figure S5b), while the correlation between relative far-red SIF and GPP/PAR is weaker (R^2 = 0.07; Figure S5a).

3.3 Detectability of Mid-summer Ecosystem Stress

While there were clear stress-induced decreases in GPP inferred from eddy covariance in August 2018 (Figure 2a; Section 3.1) coinciding with severe drought as classified by USDM (Svoboda et al., 2002; accessed via http://droughtmonitor.unl.edu), these intraseasonal stress dynamics were not obvious in remote sensing observations of SIF irradiances from PhotoSpec. Variations in red and far-red SIF irradiances followed synoptic-scale patterns in downwelling PAR (Figure 2a-b, e-f) rather than changes in GPP. Only relative red and far-red SIF values showed a notable change coinciding with the mid-summer drought, which dipped to a local minimum in mid-August (Figure 2c). Optical vegetation indices, including NDVI, Chlorophyll$_{RS}$, and PRI, remained constant over the course of the growing season (Figure 2i-j), indicating limited changes in chlorophyll and carotenoid pigments within the canopy.

To further investigate potential influences of drought stress on canopy SIF, we linearly detrended peak growing season observations (between July 15 and September 15, 2018) to distinguish intraseasonal variability from seasonal trends. We then calculated 5-day binned averages of observed data over the course of the August 2018 drought (Figure 6), and calculated correlation coefficients between detrended GPP and other variables over this period using both daily and 5-day binned data (Table 2). GPP first experienced a decline around August 10 and recovers roughly 20 days later, but the far-red and red SIF irradiances exhibited higher (instead of lower) values over these 20 days (Figure 6a). The higher SIF irradiances during a cloud- and precipitation-free period was consistent with the strong relationship with PAR demonstrated above, however relative red and far-red SIF signals were more sensitive to ecosystem stress and saw local minimum values during the second 5-day period of the drought (August 14-18; Figure 6b). Relative far-red SIF was the only variable to show a statistically significant ($p < 0.01$) correlation with GPP at both daily and 5-day temporal scales, but did not exhibit significant correlations with GPP/PAR, our LUE proxy, at daily ($R = -0.17$) or 5-day ($R = 0.08$) scales. Relative red SIF, however, showed a strong correlation with GPP/PAR at both daily ($R = 0.69$) and 5-day ($R = 0.87$) temporal scales. In contrast to Wohlfahrt et al. (2018), our observations did not show a strong red:far-red SIF ratio response to drought-induced stress (Figure 6a, c; discussed further in Section 4.3), but instead the detrended daily SIF ratio was strongly anticorrelated ($R^2 = 0.79$) with PAR. Diurnal stress-induced effects were also not seen in the 90-minute-aggregated observations of the red:far-red SIF ratio (Figure S6). We note that there was a delayed increase in PRI following the drought by ~10 days (Figure 6), which may indicate an increase in carotenoid pigments resulting from the drought period; however, we did not observe any corresponding changes in $\mathrm{Chlorophyll_{RS}}$ (Figure 6d).

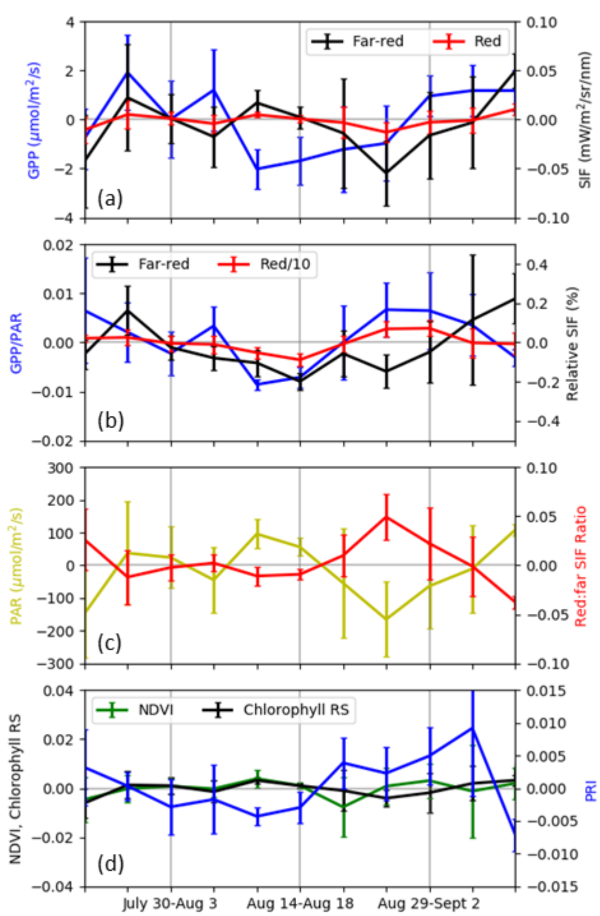

Figure 6. Five-day binned and detrended data showing GPP and SIF irradiances (a), GPP/PAR and relative SIF (b), the red:far-red SIF ratio and PAR (c), and NDVI, $\mathrm{Chlorophyll_{RS}}$, and PRI (d) during drought conditions in August 2018. Error bars represent the standard deviation of each five-day bin.

Table 2. R-values resulting from linear fits between detrended GPP and other variables between July 15 and September 15, 2018 for both daily and 5-day binned observations. Values in bold indicate statistically significant fits ($p < 0.01$).

	Daily GPP	5-day binned GPP
Far-red SIF	**0.51**	0.31
Red SIF	**0.51**	0.29
Relative Far-red SIF	**0.56**	**0.76**
Relative Red SIF	0.20	0.43
Red:Far-red SIF Ratio	**-0.41**	-0.27
PAR	**0.39**	0.10
NDVI	0.15	0.12
$Chlorophyll_{RS}$	**0.37**	0.17
PRI	0.05	0.15

3.4 Comparison with Space-based SIF from OCO-2

The ultimate goal of our tower-based SIF observations is to improve the interpretation of space-based, global SIF observations. We compared daily averages of far-red SIF observations from PhotoSpec with mean estimates of daily-averaged SIF from the OCO-2 satellite (Figure 7). The OCO-2 satellite observations were well correlated with our tower observations ($R^2 = 0.79$) showing that both sets of observations captured proportionally similar patterns in the SIF signal. However, the slope between the two datasets of 2.2 ± 0.4, reflected that the raw SIF irradiance measured by OCO-2 was twice that measured by PhotoSpec. The lower irradiance values observed by our PhotoSpec instrument likely resulted from including observations with larger incident angles between solar and viewing directions, due to including elevation angles up to 45° below horizon in the calculation of daily-averaged SIF, as well as deploying the telescope on the south side of the tower. Thus, our tower-based observations included a greater fraction of shaded vegetation because illumination and viewing angles were often from opposing cardinal directions. These differences highlight that, while tower- and space-based platforms capture similar relative patterns in SIF signals, more comprehensive comparisons between SIF observations require a more complex study of viewing and illumination angle sensitivities in top-of-canopy SIF observations.

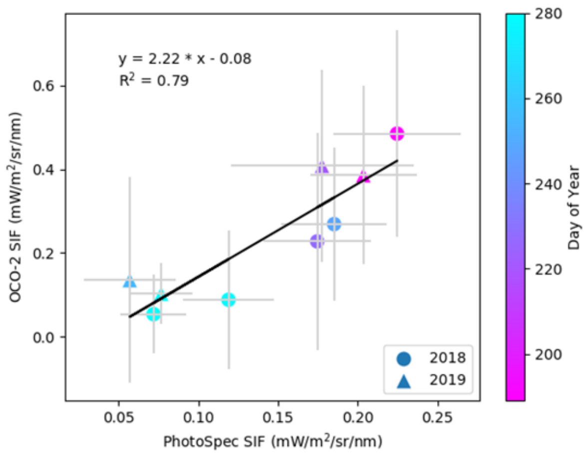

Figure 7. Correlation plot and linear fit results between far-red SIF observations from PhotoSpec and the OCO-2 satellite. OCO-2 data includes soundings within a one-degree gridcell centered at US-UMB. Each sounding was multiplied by a daily correction factor, which uses a clear-sky proxy to account for diurnal changes in the SIF signal. Means were calculated from soundings across individual days, and error bars represent the standard deviation of included observations. Mean daily values from OCO-2 were then correlated with the daily-average SIF signal seen from the PhotoSpec instrument, where uncertainties were propagated from the standard deviation of 20 s observations included in every sub-daily 90-minute average. Circles indicate data from 2018 and triangles indicate 2019. The color bar is weighted by day of year.

4 Discussion

4.1 Dependence of SIF and GPP on PAR

While our results align with several studies that suggest that high correlations between SIF and GPP primarily result from a shared dependence on absorbed radiation or APAR (Wohlfahrt et al., 2018; K. Yang et al., 2018), our findings also support many studies that have demonstrated that GPP can be estimated from SIF observations from either satellite (Guanter et al., 2012; Sun et al., 2017) or tower (Magney, Bowling, et al., 2019; Pierrat et al., 2022; X. Yang et al., 2015). That the linear relationship between SIF and GPP is largely driven by APAR is illustrated by stronger correlations between daily-averaged GPP with far-red SIF during spring and fall months (Figure 4) when canopy changes drive large swings in fPAR. The strong dependence of SIF on APAR also likely explains why correlations between far-red SIF and GPP were stronger for weekly-averaged data (which are sensitive to seasonal light variability, but average away changes driven by clouds and weather) than for daily-averaged data (which reflect both seasonal and cloud/weather-driven variations in light; Figure 3). However, the decrease in relative SIF values during the August 2018 drought (Figure 2a, c) demonstrate that SIF signals, when normalized by light levels, may reflect changes in productivity that are independent from APAR. This was confirmed by shared intraseasonal patterns between GPP/PAR, an LUE proxy, and relative SIF (Figure 2c, d), and the strong correlation between detrended GPP/PAR and relative red SIF during the August 2018 drought. These findings echo X. Yang et al. (2015) who also showed that SIF provided information related to LUE above another temperate deciduous location at Harvard Forest (US-Ha1).

We showed that SIF is more closely tied to APAR than to GPP at our site through the fact that daily-averaged SIF data were more strongly correlated with downwelling PAR (R^2 = 0.90; Figure 5a), which was roughly proportional to APAR during peak summer conditions with near-constant NDVI, than it was with GPP (R^2 = 0.61; Figure 3b). Given that the correlation between GPP and PAR was significantly weaker (R^2 = 0.51; Figure 5b), these results demonstrate the challenges in using direct SIF observations to detect changes in LUE as they may not be an effective indicator of synoptic-scale changes in productivity under mid-season conditions where canopy structure and fPAR remain relatively stable. These results contrast with the findings of X. Yang et al. (2015) who found only slightly weaker correlations between SIF and GPP than between SIF and APAR at US-Ha1. US-Ha1 is, however, more radiation-limited than is US-UMB (Wozniak et al., 2020), which would explain a closer coupling between variations in radiation and GPP at their site. Our results are in line with those of K. Yang et al. (2018), who found that SIF is a better indicator of APAR than of GPP albeit over a rice paddy. The different relationships among SIF, GPP, and PAR in these three studies indicate that SIF-derived estimates of productivity may not be free from the need for additional inputs, such as meteorological conditions that may signal ecosystem stress (as have been used for NDVI-derived estimates of GPP; see Running et al., 2004), but also that the necessity of these additional inputs is likely influenced by whether ecosystem productivity is limited by water, temperature, or radiation. At our site, we showed that relative far-red SIF responded to water stress and served as a better proxy than SIF irradiances for seasonally detrended GPP during severe drought, however this was only the case under water-limited conditions. Furthermore, as relative far-red SIF tracked productivity only during drought conditions where SIF and PAR were decoupled from GPP, we could not derive a simple regression model that combined absolute and relative SIF observations to reflect both stressed and non-stressed conditions. Future studies should investigate the necessity of using ancillary data or relative SIF to model GPP from space-based SIF observations across ecosystems comprised of various plant types and also characterized by various productivity limiting factors.

4.2 Relationship between SIF and Ecosystem Productivity

One key finding from this study is the variable relationship between far-red SIF and GPP over the course of the growing season, with the linear slope between 90-minute far-red SIF and GPP decreasing over the course of the growing season (Figure 4a). While a seasonally changing relationship between SIF and productivity has been noted in previous studies (e.g. K. Yang et al., 2018), these studies occurred over cropland where such changes could be attributed to structural changes among different phenological stages. While we see the most drastic changes in spring when there is rapid structural change, we show that the SIF:GPP relationship above a temperate deciduous forest continues to evolve after the emergence of a well-developed canopy when changes in canopy structure are minimal. The higher SIF:GPP slope in spring suggests that assuming constant proportionality may lead to an overestimate of productivity in springtime, or an underestimate in fall, when converting SIF to GPP based on an annual mean slope. Butterfield et al. (2020) showed that interannual variability in satellite-based SIF observations is higher in spring and is in better agreement with optical vegetation indices, whereas IAV in fall SIF is small and only weakly correlated with other remote sensing products. The seasonal decline in the

SIF:GPP relationship could partly explain this phenomenon since it suggests that late-season observations are characterized by a lower signal (and thus a lower signal-to-noise ratio) than are spring data, potentially obscuring IAV. The decrease in the SIF:GPP slope as the growing season progresses (Figure 4a) may be due to leaf age effects that impart subtle changes in the canopy. Specifically, if leaves wilt or shrivel as they age due to progressive water stress, absorption of PAR may shift slightly deeper into the canopy where f_{esc} is lower, thus leading to lower top-of-canopy SIF. In the future, observations of leaf area and angle distribution over the course of the growing season, in combination with canopy radiative transfer modeling, may help to further elucidate the drivers of seasonal changes in the SIF:GPP slope.

The challenges of using SIF to estimate productivity under stable canopy conditions were further illustrated by the limited response of red or far-red SIF irradiances to summer declines in GPP. When GPP declined in response to drought conditions in August 2018, SIF signals continued to reflect changes in radiation. Wohlfahrt et al. (2018) similarly found that SIF signals in a Mediterranean pine forest exhibited poor correlation with GPP during a heat wave, although their data indicated that that top-of-canopy SIF signals eventually declined in response to losses in productivity. Marrs et al. (2020) also found that SIF signals in individual deciduous species did not exhibit an immediate response to induced water stress. Yet, we found that relative far-red SIF tracks stress-induced changes in GPP more effectively than SIF irradiances and various vegetation indices over both daily and 5-day timescales, and that relative red SIF consistently mirrored synoptic-scale changes in GPP/PAR, indicating that SIF observations do capture changes in GPP and LUE when isolated from their dependence on PAR. While PAR levels in Wohlfahrt et al. (2018) were largely consistent from day to day, indicating that SIF irradiances should have been roughly proportional to relative SIF, we note the differences in timescale between our two studies (i.e., the heatwave in their study occurred over a period of 8 days while our observations captured the effects of longer-term, cumulative drought stress).

4.3 Applications of the Red:Far-red SIF Ratio

Our results show that the red:far-red SIF ratio is sensitive to changes in downwelling PAR as well as canopy structure at both seasonal and interannual scales. Similar to Magney, Frankenberg, et al. (2019), we saw considerably higher red:far-red ratios during early spring canopy development, and in late fall as canopy chlorophyll content dropped, and as lower leaf area and decreased chlorophyll content lead to decreased reabsorption of red SIF by the canopy. The red:far-red SIF ratio showed significant differences between 2018 and 2019, with 2018 ratios being slightly lower than in 2019. These year-to-year differences in the red:far-red SIF ratio are very likely explained by 2018 having greater NDVI and LAI values (see section 3.2), in turn leading to variations in the canopy escape ratio for red fluorescence on interannual timescales. However, we also showed that the red:far-red SIF ratio is highly correlated with downwelling PAR (Figure 6c), suggesting that it is also dependent on light conditions that are independent of canopy traits. These results highlight the value in simultaneous retrievals of SIF at multiple wavelengths, which are becoming increasingly available from satellites such as TROPOMI (Köhler et al., 2020), but also demonstrate that the interpretation of SIF observations at multiple wavelengths must be cognizant of differences in sensitivity to ecosystem and environmental changes on synoptic, seasonal, and interannual timescales.

Our results highlight the difficulty in leveraging the red:far-red SIF ratio to detect ecosystem stress. Magney, Frankenberg, et al. (2019) showed that stressed conditions lead to a lower red:far-red ratio at the leaf level, but that these leaf-level changes in NPQ were not noticeable in canopy-level measurements. In contrast, Wohlfahrt et al. (2018) observed an increase in the red:far-red ratio coinciding with a heat wave, and hypothesized that the contrasting response of SIF at different wavelengths may have been due to a decrease in chlorophyll content leading to less reabsorption of red fluorescence. Our results generally corroborated Magney, Frankenberg, et al. (2019; see their Figure 7b, our Figure S6), and showed that while the red:far-red SIF ratio at canopy-scale does reflect seasonal and interannual changes in canopy structure, it is also influenced by changes in downwelling PAR (Figure 6c). Thus, further studies into the response of the red:far-red SIF ratio to environmental stress would require a detailed analysis of both the influence of phenological changes in canopy structure as well as incoming light conditions on top-of-canopy SIF observations. These analyses necessitate that observations be made at high temporal frequency since year-to-year or even month-to-month changes are primarily driven by changes in canopy structure that are independent from environmental stress, as well as the incorporation of canopy radiative transfer modeling.

5 Conclusions

We deployed a PhotoSpec system with two high spectral resolution spectrometers to measure red and far-red SIF to a deciduous forest in northern Michigan. Results from the first two years of data acquisition showed that SIF signals over a temperate deciduous forest are more strongly related to radiation than to photosynthetic productivity. While a shared dependence on PAR did result in a significant correlation between SIF and GPP, the slope of this linear relationship gradually decreased over the course of the growing season, indicating that temporal changes in the far-red SIF:GPP ratio should be considered when using SIF to assess ecosystem productivity.

Our study demonstrates challenges in using SIF irradiances to detect short-term stress-induced declines in ecosystem productivity. Nonetheless, we show that observations of relative SIF may be a more reliable indicator of ecosystem stress, indicating that SIF signals do respond to stress-induced changes in productivity and track changes in LUE after accounting for changes in solar radiation. Additionally, we show that the red:far-red SIF ratio is sensitive to seasonal and interannual changes in canopy structure. Our results point to the need for coordinated multi-scale studies on the relationship between SIF and photosynthesis including at the leaf and canopy level, especially under conditions of environmental stress.

Acknowledgments

We acknowledge funding for this research provided by NASA (grant numbers 80NSSC17K0116 and 80NSSC21K1070). Funding for the US-UMB core site was provided by the U.S. Department of Energy’s Office of Science. We also acknowledge Jochen Stutz and his team at the University of California Los Angeles, as well as the Space Physics Research Laboratory at the University of Michigan, for their assistance with the construction of the PhotoSpec instrument.

Open Research

SIF and other PhotoSpec data are available at https://doi.org/10.7302/sx8c-y281. AmeriFlux environmental and eddy flux data are available at https://doi.org/10.17190/AMF/1246107. OCO-2 SIF data are available at https://doi.org/10.5067/XO2LBBNPO010.

References

Aron, P. G., Poulsen, C. J., Fiorella, R. P., & Matheny, A. M. (2019). Stable Water Isotopes Reveal Effects of Intermediate Disturbance and Canopy Structure on Forest Water Cycling. Journal of Geophysical Research: Biogeosciences, 124(10), 2958–2975.

Beck, P. S. A., Atzberger, C., Høgda, K. A., Johansen, B., & Skidmore, A. K. (2006). Improved monitoring of vegetation dynamics at very high latitudes: A new method using MODIS NDVI. Remote Sensing of Environment, 100(3), 321–334.

Butterfield, Z., Buermann, W., & Keppel-Aleks, G. (2020). Satellite observations reveal seasonal redistribution of northern ecosystem productivity in response to interannual climate variability. Remote Sensing of Environment, 242, 111755.

Butterfield, Z., Muccio, D., Keppel-Aleks, G. (2022). Tower observations of solar-induced chlorophyll fluorescence at the University of Michigan Biological Station, University of Michigan - Deep Blue Data, (Dataset). https://doi.org/10.7302/sx8c-y281

Datt, B. (1999). A new reflectance index for remote sensing of chlorophyll content in higher plants: Tests using Eucalyptus leaves. Journal of Plant Physiology, 154(1), 30–36. https://doi.org/10.1016/S0176-1617(99)80314-9

Dechant, B., Ryu, Y., Badgley, G., Zeng, Y., Berry, J. A., Zhang, Y., Goulas, Y., Li, Z., Zhang, Q., & Kang, M. (2020). Canopy structure explains the relationship between photosynthesis and sun-induced chlorophyll fluorescence in crops. Remote Sensing of Environment, 241, 111733.

Fotis, A. T., Morin, T. H., Fahey, R. T., Hardiman, B. S., Bohrer, G., & Curtis, P. S. (2018). Forest structure in space and time: Biotic and abiotic determinants of canopy complexity and their effects on net primary productivity. Agricultural and Forest Meteorology, 250, 181–191.

Frankenberg, C., Butz, A., & Toon, G. C. (2011). Disentangling chlorophyll fluorescence from atmospheric scattering effects in O2 A-band spectra of reflected sun-light. Geophysical Research Letters, 38(3).

Frankenberg, C., Fisher, J. B., Worden, J., Badgley, G., Saatchi, S. S., Lee, J., Toon, G. C., Butz, A., Jung, M., & Kuze, A. (2011). New global observations of the terrestrial carbon cycle from GOSAT: Patterns of plant fluorescence with gross primary productivity. Geophysical Research Letters, 38(17).

Frankenberg, C., O'Dell, C., Berry, J., Guanter, L., Joiner, J., Köhler, P., Pollock, R., & Taylor, T. E. (2014). Prospects for chlorophyll fluorescence remote sensing from the Orbiting Carbon Observatory-2. Remote Sensing of Environment, 147, 1–12.

Frasson, R. P. de M., Bohrer, G., Medvigy, D., Matheny, A. M., Morin, T. H., Vogel, C. S., Gough, C. M., Maurer, K. D., & Curtis, P. S. (2015). Modeling forest carbon cycle response to tree mortality: effects of plant functional type and disturbance intensity. Journal of Geophysical Research: Biogeosciences, 120(11), 2178–2193.

Friedlingstein, P., Jones, M. W., O'Sullivan, M., Andrew, R. M., Bakker, D. C. E., Hauck, J., le Quéré, C., Peters, G. P., Peters, W., & Pongratz, J. (2022). Global carbon budget 2021. Earth System Science Data, 14(4), 1917–2005.

Gamon, J. A., Field, C. B., Fredeen, A. L., & Thayer, S. (2001). Assessing photosynthetic downregulation in sunflower stands with an optically-based model. Photosynthesis Research, 67(1–2), 113–125.

Gitelson, A. A., & Gamon, J. A. (2015). The need for a common basis for defining light-use efficiency: Implications for productivity estimation. Remote Sensing of Environment, 156, 196–201.

Gough, C. M., Bohrer, G., & Curtis, P. (2022). AmeriFlux BASE US-UMB Univ. of Mich. Biological Station, Ver. 18-5. AmeriFlux AMP, (Dataset). https://doi.org/10.17190/AMF/1246107

Gough, C. M., Hardiman, B. S., Nave, L. E., Bohrer, G., Maurer, K. D., Vogel, C. S., Nadelhoffer, K. J., & Curtis, P. S. (2013). Sustained carbon uptake and storage following moderate disturbance in a Great Lakes forest. Ecological Applications, 23(5), 1202–1215.

Grossmann, K., Frankenberg, C., Magney, T. S., Hurlock, S. C., Seibt, U., & Stutz, J. (2018). Remote Sensing of Environment PhotoSpec : A new instrument to measure spatially distributed red and far- red Solar-Induced Chlorophyll Fluorescence. Remote Sensing of Environment, 216(June), 311–327. https://doi.org/10.1016/j.rse.2018.07.002

Guanter, L., Frankenberg, C., Dudhia, A., Lewis, P. E., Gómez-Dans, J., Kuze, A., Suto, H., & Grainger, R. G. (2012). Retrieval and global assessment of terrestrial chlorophyll fluorescence from GOSAT space measurements. Remote Sensing of Environment, 121, 236–251.

He, L., Ivanov, V. Y., Bohrer, G., Maurer, K. D., Vogel, C. S., & Moghaddam, M. (2014). Effects of fine-scale soil moisture and canopy heterogeneity on energy and water fluxes in a northern temperate mixed forest. Agricultural and Forest Meteorology, 184, 243–256.

Joiner, J., Guanter, L., Lindstrot, R., Voigt, M., Vasilkov, A. P., Middleton, E. M., Huemmrich, K. F., Yoshida, Y., & Frankenberg, C. (2013). Global monitoring of terrestrial chlorophyll fluorescence from moderate-spectral-resolution near-infrared satellite measurements: methodology, simulations, and application to GOME-2. Atmospheric Measurement Techniques, 6(10), 2803–2823.

Köcher, P., Gebauer, T., Horna, V., & Leuschner, C. (2009). Leaf water status and stem xylem flux in relation to soil drought in five temperate broad-leaved tree species with contrasting water use strategies. Annals of Forest Science, 66(1), 1.

Köhler, P., Behrenfeld, M. J., Landgraf, J., Joiner, J., Magney, T. S., & Frankenberg, C. (2020). Global Retrievals of Solar-Induced Chlorophyll Fluorescence at Red Wavelengths With TROPOMI. Geophysical Research Letters, 47(15), e2020GL087541.

Köhler, P., Frankenberg, C., Magney, T. S., Guanter, L., Joiner, J., & Landgraf, J. (2018). Global Retrievals of Solar-Induced Chlorophyll Fluorescence With TROPOMI: First Results and Intersensor Comparison to OCO-2. Geophysical Research Letters, 45(19), 10–456.

Lascano, R., Sojka, R. E., & Evett, S. (2007). Soil Water and Monitoring Technology. https://doi.org/10.2134/agronmonogr30.2ed.c2

Lasslop, G., Reichstein, M., Papale, D., Richardson, A. D., Arneth, A., Barr, A., Stoy, P., & Wohlfahrt, G. (2010). Separation of net ecosystem exchange into assimilation and respiration using a light response curve approach: critical issues and global evaluation. Global Change Biology, 16(1), 187–208.

le Quéré, C., Andrew, R. M., Friedlingstein, P., Sitch, S., Pongratz, J., Manning, A. C., Korsbakken, J. I., Peters, G. P., Canadell, J. G., Jackson, R. B., Boden, T. A., Tans, P. P., Andrews, O. D., Arora, V. K., Bakker, D. C. E., Barbero, L., Becker, M., Betts, R. A., Bopp, L., … Zhu, D. (2018). Global Carbon Budget 2017. Earth Syst. Sci. Data, 10, 405–448. https://doi.org/10.5194/essd-10-405-2018

Li, X., Xiao, J., Kimball, J. S., Reichle, R. H., Scott, R. L., Litvak, M. E., Bohrer, G., & Frankenberg, C. (2020). Synergistic use of SMAP and OCO-2 data in assessing the responses of ecosystem productivity to the 2018 US drought. Remote Sensing of Environment, 251, 112062.

Magney, T. S., Barnes, M. L., & Yang, X. (2020). On the covariation of chlorophyll fluorescence and photosynthesis across scales. Geophysical Research Letters, 47(23), e2020GL091098.

Magney, T. S., Bowling, D. R., Logan, B. A., Grossmann, K., Stutz, J., Blanken, P. D., Burns, S. P., Cheng, R., Garcia, M. A., & Köhler, P. (2019). Mechanistic evidence for tracking the seasonality of photosynthesis with solar-induced fluorescence. Proceedings of the National Academy of Sciences, 116(24), 11640–11645.

Magney, T. S., Frankenberg, C., Köhler, P., North, G., Davis, T. S., Dold, C., Dutta, D., Fisher, J. B., Grossmann, K., & Harrington, A. (2019). Disentangling changes in the spectral shape of chlorophyll fluorescence: Implications for remote sensing of photosynthesis. Journal of Geophysical Research: Biogeosciences, 124(6), 1491–1507.

Marrs, J. K., Reblin, J. S., Logan, B. A., Allen, D. W., Reinmann, A. B., Bombard, D. M., Tabachnik, D., & Hutyra, L. R. (2020). Solar-Induced Fluorescence Does Not Track Photosynthetic Carbon Assimilation Following Induced Stomatal Closure. Geophysical Research Letters, 47(15), e2020GL087956.

Matheny, A. M., Bohrer, G., Vogel, C. S., Morin, T. H., He, L., Frasson, R. P. de M., Mirfenderesgi, G., Schäfer, K. V. R., Gough, C. M., & Ivanov, V. Y. (2014). Species-specific transpiration responses to intermediate disturbance in a northern hardwood forest. Journal of Geophysical Research: Biogeosciences, 119(12), 2292–2311.

Matheny, A. M., Fiorella, R. P., Bohrer, G., Poulsen, C. J., Morin, T. H., Wunderlich, A., Vogel, C. S., & Curtis, P. S. (2017). Contrasting strategies of hydraulic control in two codominant temperate tree species. Ecohydrology, 10(3), e1815.

Miao, G., Guan, K., Yang, X., Bernacchi, C. J., Berry, J. A., DeLucia, E. H., Wu, J., Moore, C. E., Meacham, K., & Cai, Y. (2018). Sun-induced chlorophyll fluorescence, photosynthesis, and light use efficiency of a soybean field from seasonally continuous measurements. Journal of Geophysical Research: Biogeosciences, 123(2), 610–623.

Monteith, J. L. (1977). Climate and the efficiency of crop production in Britain. Philosophical Transactions of the Royal Society of London. B, Biological Sciences, 281(980), 277–294.

Morin, T. H., Bohrer, G., Frasson, R. P. d M., Naor-Azreli, L., Mesi, S., Stefanik, K. C., & Schäfer, K. V. R. (2014). Environmental drivers of methane fluxes from an urban temperate wetland park. Journal of Geophysical Research: Biogeosciences, 119(11), 2188–2208.

Pierrat, Z., Magney, T., Parazoo, N. C., Grossmann, K., Bowling, D. R., Seibt, U., Johnson, B., Helgason, W., Barr, A., & Bortnik, J. (2022). Diurnal and Seasonal Dynamics of Solar-Induced Chlorophyll Fluorescence, Vegetation Indices, and Gross Primary Productivity in the Boreal Forest. Journal of Geophysical Research: Biogeosciences, 127(2), e2021JG006588.

Rebmann, C., Kolle, O., Heinesch, B., Queck, R., Ibrom, A., & Aubinet, M. (2012). Data acquisition and flux calculations. In Eddy covariance (pp. 59–83). Springer.

Reichstein, M., Falge, E., Baldocchi, D., Papale, D., Aubinet, M., Berbigier, P., Bernhofer, C., Buchmann, N., Gilmanov, T., & Granier, A. (2005). On the separation of net ecosystem exchange into assimilation and ecosystem respiration: review and improved algorithm. Global Change Biology, 11(9), 1424–1439.

Running, S. W., Nemani, R. R., Heinsch, F. A., Zhao, M., Reeves, M., & Hashimoto, H. (2004). A continuous satellite-derived measure of global terrestrial primary production. AIBS Bulletin, 54(6), 547–560.

Ryu, Y., Berry, J. A., & Baldocchi, D. D. (2019). What is global photosynthesis? History, uncertainties and opportunities. Remote Sensing of Environment, 223, 95–114.

Science Team, O.-2, Gunson, M., & Eldering, A. (2017). OCO-2 Level 2 bias-corrected solar-induced fluorescence and other select fields from the IMAP-DOAS algorithm aggregated as daily files, Retrospective processing V8r. Goddard Earth Sciences Data and Information Services Center (GES DISC). 10.5067/AJMZO5O3TGUR

Song, L., Guanter, L., Guan, K., You, L., Huete, A., Ju, W., & Zhang, Y. (2018). Satellite sun-induced chlorophyll fluorescence detects early response of winter wheat to heat stress in the Indian Indo-Gangetic Plains. Global Change Biology, 24(9), 4023–4037.

Sun, Y., Frankenberg, C., Jung, M., Joiner, J., Guanter, L., Köhler, P., & Magney, T. (2018). Overview of Solar-Induced chlorophyll Fluorescence (SIF) from the Orbiting Carbon Observatory-2: Retrieval, cross-mission comparison, and global monitoring for GPP. Remote Sensing of Environment, 209, 808–823.

Sun, Y., Frankenberg, C., Wood, J. D., Schimel, D. S., Jung, M., Guanter, L., Drewry, D. T., Verma, M., Porcar-Castell, A., & Griffis, T. J. (2017). OCO-2 advances photosynthesis observation from space via solar-induced chlorophyll fluorescence. Science, 358(6360), eaam5747.

Svoboda, M., LeComte, D., Hayes, M., Heim, R., Gleason, K., Angel, J., Rippey, B., Tinker, R., Palecki, M., & Stooksbury, D. (2002). The drought monitor. Bulletin of the American Meteorological Society, 83(8), 1181–1190.

Tucker, C. J. (1979). Red and photographic infrared linear combinations for monitoring vegetation. Remote Sensing of Environment, 8(2), 127–150. https://doi.org/https://doi.org/10.1016/0034-4257(79)90013-0

Wohlfahrt, G., Gerdel, K., Migliavacca, M., Rotenberg, E., Tatarinov, F., Müller, J., Hammerle, A., Julitta, T., Spielmann, F. M., & Yakir, D. (2018). Sun-induced fluorescence and gross primary productivity during a heat wave. Scientific Reports, 8(1), 14169.

Wolanin, A., Rozanov, V. v, Dinter, T., Noël, S., Vountas, M., Burrows, J. P., & Bracher, A. (2015). Global retrieval of marine and terrestrial chlorophyll fluorescence at its red peak using hyperspectral top of atmosphere radiance measurements: Feasibility study and first results. Remote Sensing of Environment, 166, 243–261.

Wozniak, M. C., Bonan, G. B., Keppel-Aleks, G., & Steiner, A. L. (2020). Influence of Vertical Heterogeneities in the Canopy Microenvironment on Interannual Variability of Carbon

Uptake in Temperate Deciduous Forests. Journal of Geophysical Research: Biogeosciences, 125(8), e2020JG005658.

Yang, K., Ryu, Y., Dechant, B., Berry, J. A., Hwang, Y., Jiang, C., Kang, M., Kim, J., Kimm, H., & Kornfeld, A. (2018). Sun-induced chlorophyll fluorescence is more strongly related to absorbed light than to photosynthesis at half-hourly resolution in a rice paddy. Remote Sensing of Environment, 216, 658–673.

Yang, X., Tang, J., Mustard, J. F., Lee, J., Rossini, M., Joiner, J., Munger, J. W., Kornfeld, A., & Richardson, A. D. (2015). Solar-induced chlorophyll fluorescence that correlates with canopy photosynthesis on diurnal and seasonal scales in a temperate deciduous forest. Geophysical Research Letters, 42(8), 2977–2987.

Yazbeck, T., Bohrer, G., Gentine, P., Ye, L., Arriga, N., Bernhofer, C., Blanken, P. D., Desai, A. R., Durden, D., & Knohl, A. (2021). Site Characteristics Mediate the Relationship Between Forest Productivity and Satellite Measured Solar Induced Fluorescence. Frontiers in Forests and Global Change, 193.

Yoshida, Y., Joiner, J., Tucker, C., Berry, J., Lee, J.-E., Walker, G., Reichle, R., Koster, R., Lyapustin, A., & Wang, Y. (2015). The 2010 Russian drought impact on satellite measurements of solar-induced chlorophyll fluorescence: Insights from modeling and comparisons with parameters derived from satellite reflectances. Remote Sensing of Environment, 166, 163–177.

Yu, L., Wen, J., Chang, C. Y., Frankenberg, C., & Sun, Y. (2019). High-resolution global contiguous SIF of OCO-2. Geophysical Research Letters, 46(3), 1449–1458.

Zeng, Y., Badgley, G., Dechant, B., Ryu, Y., Chen, M., & Berry, J. A. (2019). A practical approach for estimating the escape ratio of near-infrared solar-induced chlorophyll fluorescence. Remote Sensing of Environment, 232, 111209.

Journal of Geophysical Research - Biogeosciences

Supporting Information for

Accounting for Changes in Radiation Improves the Ability of SIF to Track Water Stress-Induced Losses in Summer GPP in a Temperate Deciduous Forest

Zachary Butterfield[1], Troy Magney[2], Katja Grossmann[3], Gil Boher[4], Chris Vogel[5], Stephen Barr[1], Gretchen Keppel-Aleks[1]

[1]Climate and Space Sciences and Engineering, University of Michigan, Ann Arbor, Michigan

[2]Department of Plant Sciences, University of California, Davis, California

[3]Institute of Environmental Physics, University of Heidelberg, Heidelberg, German

[4]Civil, Environmental and Geodetic Engineering, Ohio State University, Columbus, Ohio

[5]University of Michigan Biological Station, Pellston, Michigan

Contents of this file

Introduction

The supporting information include additional methods and results that are relevant but not critical to the conclusions of the paper. Contents include:

- a brief explanation and list of equations used to calculate vegetation indices included in the study;
- several figures that present supplemental information using similar methods as described in the main manuscript.

Text S1. Equations for calculating vegetation indices

The normalized difference vegetation index (NDVI; Tucker, 1979), photochemical reflectance index (PRI; Gamon et al., 1992), and chlorophyll index ($Chlorophyll_{RS}$; Datt, 1999; Magney et al., 2019) were calculated using the below equations using canopy reflectance observed by the broadband Flame spectrometer (Ocean Optics Inc.). R_{λ} represents the reflectance at a wavelength of λ nm, or in the red (620-670 nm) or near-infrared (NIR; 830-860 nm) regions of the electromagnetic spectrum.

$$NDVI = (R_{NIR} – R_{Red})/(R_{NIR} + R_{Red}) \quad (S1)$$

$$PRI = (R_{531} – R_{570})/(R_{531} – R_{570}) \quad (S2)$$

$$Chlorophyll_{RS} = (R_{850} – R_{710})/(R_{850} – R_{680}) \quad (S3)$$

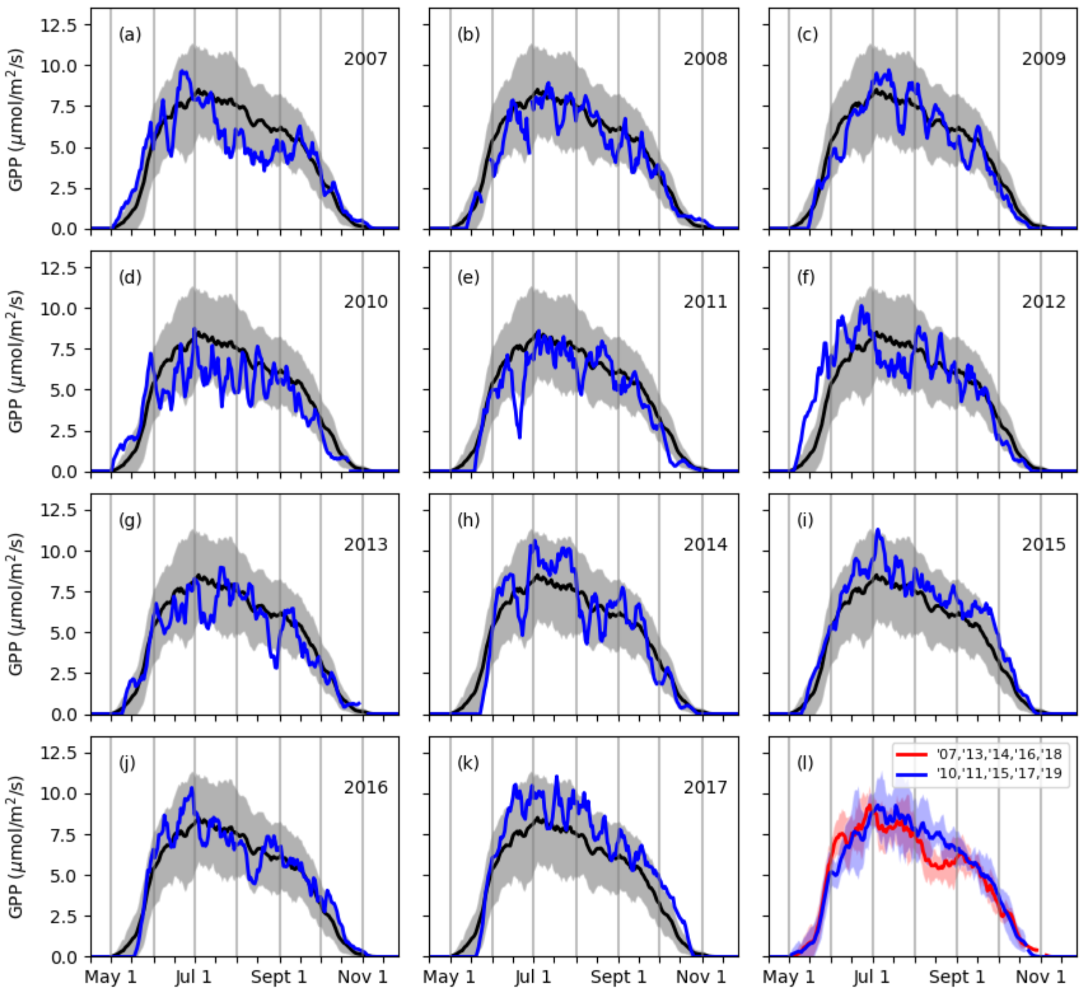

Figure S1. Observations of gross primary productivity (GPP) at US-UMB for 2007-2017 (a-k) and composite means of years with and without late-summer dips in productivity (l). In panel l, the mean of 2007, 2013, 2014, 2016, and 2018 is shown in red as years experiencing summer losses in productivity, while the mean of 2010, 2011, 2015, 2017, and 2019 is shown in blue as years that did not see summer losses (see also Figure 1a). The black line in panels a-k represents the 2007-2019 multi-year mean. Shading in all panels represents ±1 standard deviation of the respective multi-year means.

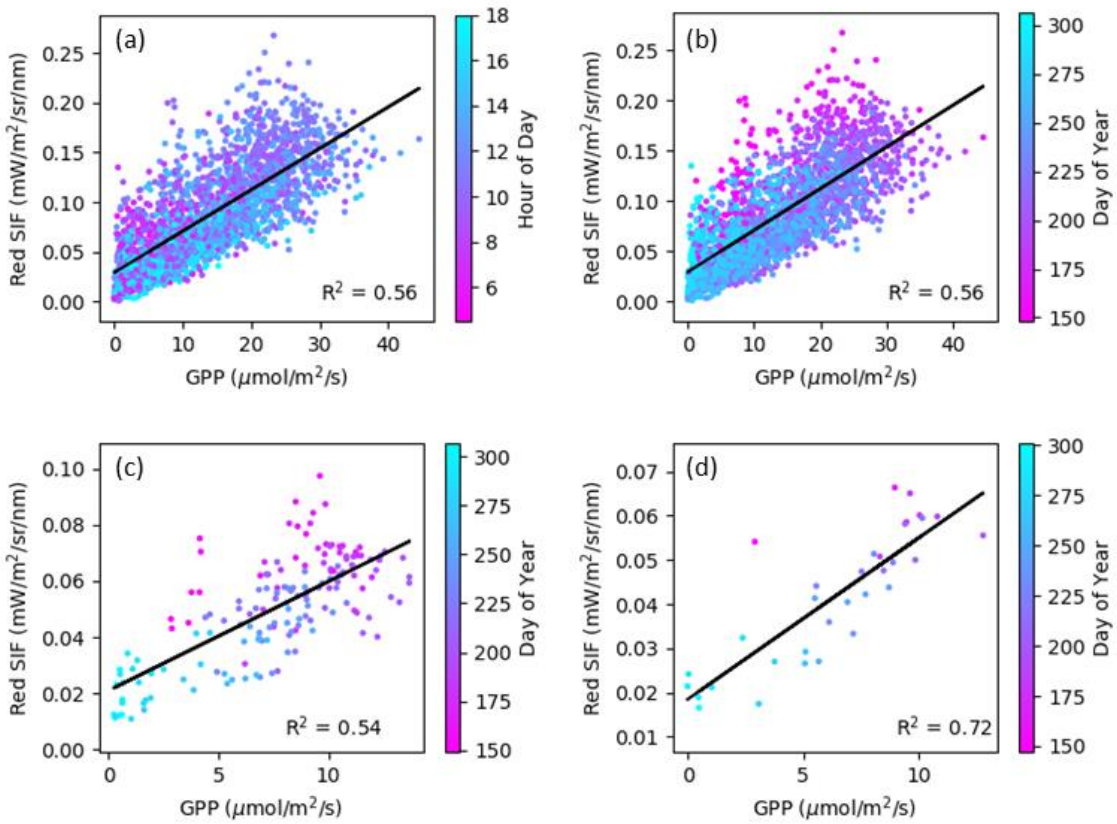

Figure S2. Correlation plots between red solar-induced chlorophyll fluorescence (SIF) and GPP at 90-minute (a, b), daily (c), and weekly (d) temporal resolution observations. Color bars are weighted by day of year (b-d) or by hour of day (a).

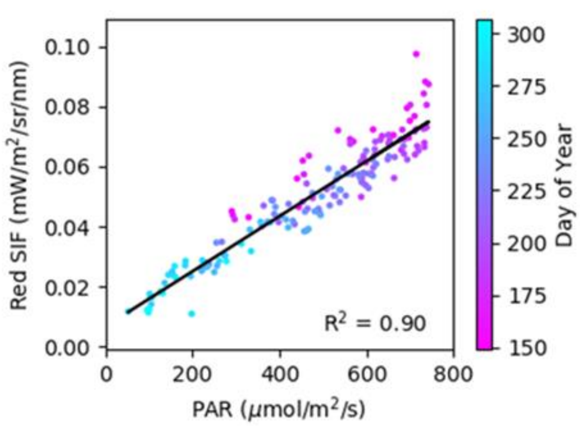

Figure S3. Correlation plot between daily-averaged red SIF and photosynthetically active radiation (PAR). Color bar is weighted by day of year.

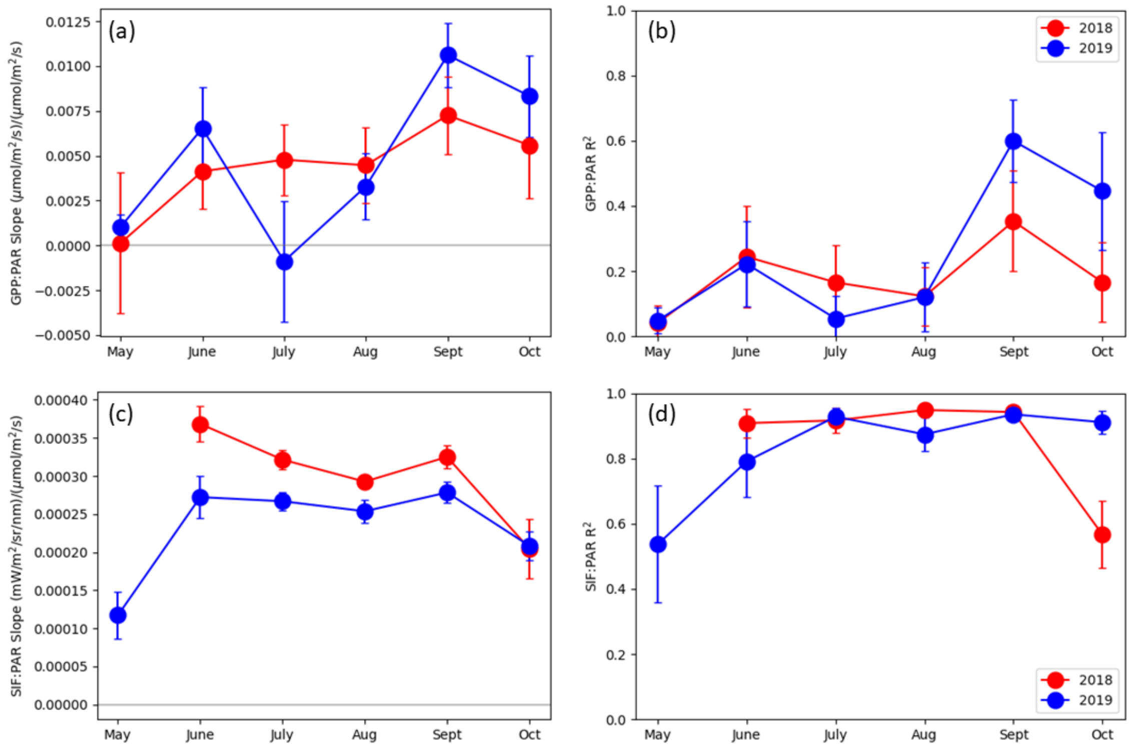

Figure S4. Slopes and correlation coefficients from monthly linear fits of daily-averaged GPP (a, b) and far-red SIF (c, d) with PAR. Data from 2018 are in red, while 2019 data are in blue. Error bars represent the standard deviations of results from a bootstrapping method used to test the robustness of the linear regressions.

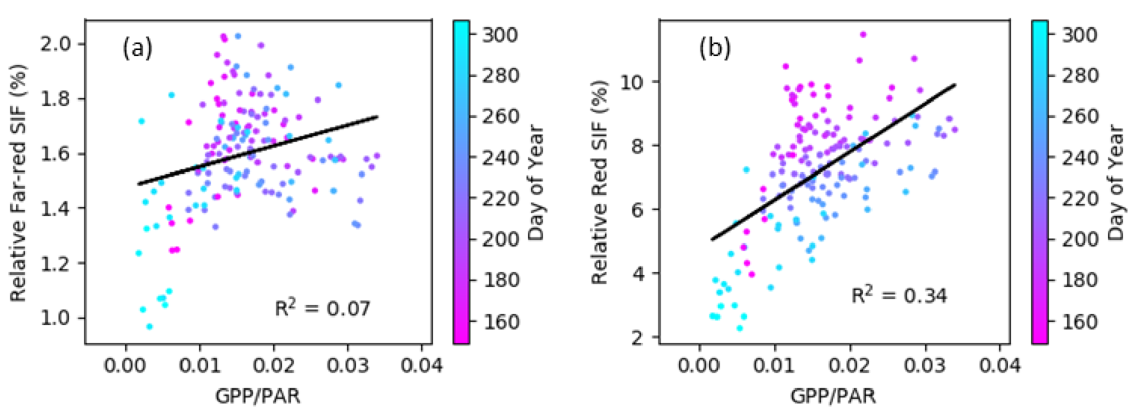

Figure S5. Correlation plot between daily-averaged relative far-red (a) and red (b) SIF and GPP/PAR, an LUE proxy. Color bar is weighted by day of year.

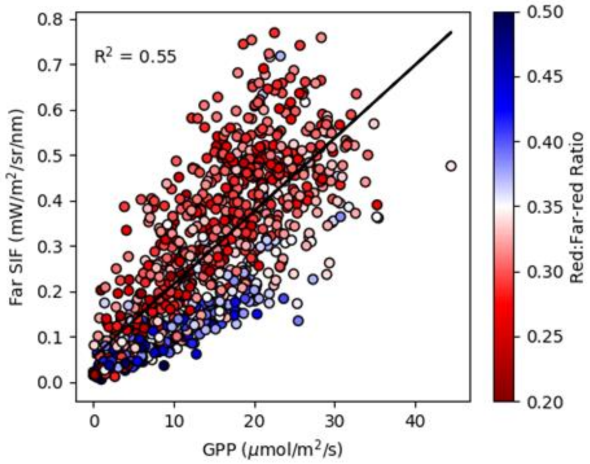

Figure S6. Correlation plot between 90-minute far-red SIF and GPP observations. Color scale is weighted by the red:far-red SIF ratio. (Compare with Figure 7b from Magney et al., 2019.)

References

Datt, B. (1999). A new reflectance index for remote sensing of chlorophyll content in higher plants: tests using Eucalyptus leaves. Journal of Plant Physiology, 154(1), 30–36.

Gamon, J. A., Penuelas, J., & Field, C. B. (1992). A narrow-waveband spectral index that tracks diurnal changes in photosynthetic efficiency. Remote Sensing of Environment, 41(1), 35–44.

Magney, T. S., Frankenberg, C., Köhler, P., North, G., Davis, T. S., Dold, C., Dutta, D., Fisher, J. B., Grossmann, K., & Harrington, A. (2019). Disentangling changes in the spectral shape of chlorophyll fluorescence: Implications for remote sensing of photosynthesis. Journal of Geophysical Research: Biogeosciences, 124(6), 1491–1507.

Tucker, C. J. (1979). Red and photographic infrared linear combinations for monitoring vegetation. Remote Sensing of Environment, 8(2), 127–150. https://doi.org/https://doi.org/10.1016/0034-4257(79)90013-0